Compressibility of zinc sulfide nanoparticles

B. Gilbert,[1] H. Zhang,[2] B. Chen,[2] M. Kunz,[3] F. Huang,[4] and J. F. Banfield[2]
[1]*Earth Sciences Division, Lawrence Berkeley National Laboratory, Berkeley, California 94720, USA*
[2]*Department of Earth & Planetary Sciences, University of California–Berkeley, Berkeley, California 94720, USA*
[3]*Advanced Light Source, Lawrence Berkeley National Laboratory, Berkeley, California 94720, USA*
[4]*Fujian Institute of Research on the Structure of Matter, Chinese Academy of Sciences, Fuzhou, Fujian 350002, People's Republic of China*

(Received 17 March 2006; revised manuscript received 18 July 2006; published 12 September 2006)

We describe a high-pressure x-ray diffraction (XRD) study of the compressibility of several samples of ZnS nanoparticles. The nanoparticles were synthesized with a range of sizes and surface chemical treatments in order to identify the factors that determine nanoparticle compressibility. Refinement of the XRD data revealed that all ZnS nanoparticles in the nominally *cubic* (sphalerite) phase exhibited a previously unobserved structural distortion under ambient conditions that exhibited, in addition, a dependence on pressure. Our results show that the compressibility of ZnS nanoparticles increases substantially as the particle size decreases, and we propose an interpretation based upon the available mechanisms of structural compliance in nanoscale vs bulk materials.

DOI: 10.1103/PhysRevB.74.115405 PACS number(s): 62.25+g, 61.10.Nz, 61.50.Ks

I. INTRODUCTION

The structure, stability, and chemical properties of materials can exhibit a strong dependence on particle size when a material is nanosized. At present, however, the relationships between the surface strain, interior structure, and the mechanical properties of nanoparticles are poorly understood. There have been many structural studies of the tetrahedrally coordinated metal-chalcogenide semiconductor nanoparticles, such as CdS, CdSe, and ZnS. Nanoparticles of these materials exemplify how competing kinetic and thermodynamic factors during synthesis affect structure. For example, in the synthesis of ZnS nanoparticles, both nucleation kinetics and surface-ligand interactions can determine whether the stable bulk phase (the *cubic* sphalerite structure), the metastable bulk phase (the *hexagonal* wurtzite structure), or a mixed-phase polytype structure is obtained.[1,2] Moreover, with the application of *in situ*, high-energy x-ray-scattering methods, we have shown that ZnS nanoparticles generally contain substantial strain and disorder[3] and that their interior structure can be changed through surface interactions.[4] For example, water binding can drive a structural transformation at room temperature; and it is possible to synthesize ~3 nm ZnS nanoparticles with a large range of interior crystallinity, correlated with the strength of surface-ligand chemical interactions.[5]

The studies described above contributed to a depiction of nanoparticle structure at ambient pressure. Investigations of the structure of nanoparticles at high pressure can provide additional insights into size-dependent changes in phase stability and mechanical properties. Specifically, relationships between nanoparticle structure and the energies of nanoparticle bulk and surface can be revealed by pressure-driven phase transitions.[6–8] In studies of CdSe nanoparticles that are smaller than the critical volume for phase transition, the wurtzite to rock salt phase-transition pressure increases with decreasing particle size. This occurs because phase transformation leads to low-index, low-energy surfaces becoming high-index, high-energy surfaces in the high-pressure phase. The same trend is observed in phase-transformation studies on ZnS nanoparticles.

There are few investigations of the response of tetrahedrally coordinated nanoparticles to pressure away from phase transitions. High-pressure x-ray-diffraction (XRD) studies can probe the elastic properties of materials, in particular, for hydrostatic experimental conditions, the bulk modulus B. The inverse of a material's compressibility, B quantifies the compression that is produced by a uniform external pressure. To date, studies of the compressibility of ZnS nanoparticles have disagreed on whether small particle size leads to higher or lower compressibility relative to the bulk material.[9,10] In the study by Pan *et al.*, 6-nm-diam wurtzite phase ZnS nanoparticles doped with Eu at 1 wt % exhibited a greater compressibility (i.e., a lower B) than bulk ZnS.[9] In the study by Qadri *et al.*, 2.8-nm-diam sphalerite ZnS nanoparticles, Mn doped at 0.5 wt % were more compressible than bulk ZnS.[10] Further work by Qadri *et al.*, however, showed a clear trend in which the compressibility of PbS nanoparticles (*rock salt* structure at ambient pressure) increased with decreasing particle size.[11]

The discrepancies between these findings are probably related to differences in the detailed structure of the nanoparticles, particularly the presence of impurity atoms. Here we seek the factors that determine the compressibility of pure ZnS nanoparticles. We used different synthesis methods to produce ZnS nanoparticles nominally in the *cubic* (sphalerite) crystal phase, but differing in size, crystallinity, and surface chemistry. In addition, we study one sample of ~4.8 nm nanoparticles in the *hexagonal* (wurtzite) phase.

II. EXPERIMENTAL

A. Nanoparticle synthesis and characterization

Zinc sulfide nanoparticles were synthesized with a variety of methods resulting in a range of particle sizes, structures,

and surface coatings. MER: 3.4-nm-diam ZnS nanoparticles coated in mercaptoethanol ($SHCH_2CH_2OH$) were synthesized by combining aqueous solutions of Na_2S and $ZnCl_2$ at pH 10.2 in the presence of mercaptoethanol (Ref. 12). WTR: ~4-nm-diam uncoated ZnS nanoparticles in water were obtained by adding dropwise a solution of 4.8 g of Na_2S in 200 ml de-ionized (DI) water to 2.7 g of $ZnCl_2$ in 300 ml DI water adjusted to pH 11 with NaOH (Ref. 13). ACE3: ~3-nm-diam ZnS nanoparticles coated in thioacetamide (CH_3CSNH_2) were synthesized by the reaction of 100 ml of a 0.02*M* thioacetamide solution with 100 ml of 0.02*M* zinc acetate in basic conditions (Ref. 14). ACE6: ~6-nm-diam ZnS nanoparticles coated in thioacetamide were obtained by hydrothermally coarsening a portion of sample ACE3 at 100 °C for 48 h. WUR: ~4.8-nm-diam ZnS nanoparticles with a hexagonal (wurtzite) structure was synthesized by the reaction of thiourea with zinc chloride in ethylene glycol at 160 °C (Ref. 2).

The particle size was estimated by an XRD peak-width broadening and checked with high-resolution transmission electron microscopy (TEM). The samples were dried before analysis, and the structures of the nanoparticles were determined with ambient-pressure XRD of the dried powders.

B. Ambient-pressure high-energy wide-angle x-ray scattering

One nanoparticle sample (MER: 3.4 nm mercaptoethanol-coated ZnS) was studied with high-energy x-ray scattering. The goal was to obtain a diffraction pattern that covers a greater range of reciprocal space to aid in the identification of a noncubic distortion that was observed in the smallest samples. A thin (<1 mm) slab of the dried powder was analyzed on beamline 11-ID-C of the Advanced Photon Source at the x-ray energy of 93 keV ($\lambda = 0.133\,31$ Å). The two-dimensional (2D) diffraction image was recorded on a Mar345 image plate,[15] and the data processing and analysis were performed as described below.

C. High-pressure x-ray-diffraction measurements

The samples were analyzed at high pressure in a membrane-style diamond anvil cell (DAC; Diacell, UK) with two independent pressure calibrants: grains of ruby (Cr-doped corundum, Al_2O_3) and a single flake of pressed gold powder. The gold diffraction rings do not overlap the rings from ZnS and permit the internal DAC pressure to be measured via changes in the gold unit-cell parameters, without dismounting the DAC from the beamline. The emission wavelengths of the optical fluorescence lines of ruby are sensitive to pressure, and the fluorescence-line profile is sensitive to the presence of nonhydrostatic pressure.[16]

Stainless-steel gaskets were preindented to 25–30 bars before electrodrilling a central, 125-μm-diam hole and mounting on one of the pair of aligned diamond anvils. The sample powder and a few grains of ruby were placed into the gasket hole. A small gold flake was added near the top or bottom of the gasket hole, ensuring no overlap with the edge of the gasket. An ambient-pressure XRD pattern was acquired for every sample mounted as described above, without a pressure medium or the DAC piston containing the second diamond.

A drop of a 4:1 mixture of methanol and ethanol was added to provide a hydrostatic pressure medium. The DAC was closed before evaporation could occur inside the gasket hole, the DAC was pressurized immediately to between 6–10 bars external pressure, and the internal pressure was measured using the ruby fluorescence lines. If at least three individual ruby grains were found that indicated a hydrostatic pressure in the range 1–3 GPa, the compressibility measurements began.

The DAC was mounted on beamline 11.3.1 of the Advanced Light Source and XRD patterns acquired on a 2D CCD detector (Bruker Platinum 200; 140 mm^2 active area) with 17 keV x rays ($\lambda = 0.729294$ Å). The DAC was centered horizontally and vertically relative to the x-ray beam and centered onto the axis of a rotation stage. The centering procedure was performed every time the DAC was mounted, and has been determined to reproduce the distance between the sample and the detector to within 20 μm. The 11.3.1 beam was collimated to reduce gasket scattering, and the beamline hutch was air conditioned to reduce temperature variations. Due to the narrow vertical x-ray beam profile, a DAC position could usually be found from which a sample only or a sample plus gold calibrant XRD patterns were acquired. In this way, separate sample and calibrant patterns were taken at each pressure point. During two ZnS compressibility experiments, a ruby-pressure measurement was taken at each pressure point to obtain the equation of state of the gold used in this study. In the other studies, ruby-pressure measurements were only taken following every increment of approximately 10 bars of external DAC pressure to check for hydrostatic conditions. The maximum internal DAC pressure reached was 12 GPa, at least 3 GPa below any anticipated phase transitions. In most experimental runs, gasket deformation occurred significantly below this pressure, ending the run.

The sample-detector distance and the detector tilt were determined from a refinement of the powder-diffraction pattern of LaB_6 (NIST) acquired at ambient pressure using the software FIT2D.[17] A previously determined spatial correction for distortion at the CCD detector was applied to all XRD patterns.[18] XRD images were binned to 1D scans,[19] using a digital mask to obscure the beamstop and ruby diffraction spots. Every image was inspected for ruby spots, and the cumulative mask was used for every image integration before analysis either with the GSAS XRD refinement package[20] or routines written in the IGOR PRO commercial software.

D. Pressure calibration

Pressure calibration with the ruby internal standard was performed by finding the emission wavelengths (λ, in nm) of the R_1 and R_2 emission lines, obtained from fits of two pseudo-Voigt peaks to the fluorescence emission spectra. The pressure P was determined for each peak by the relation $P = (\lambda - \lambda_{amb})/0.365$. The results for the R_1 and R_2 peaks were averaged. The degree of internal pressure hydrostaticity was

checked visually by the width and overlap of the R_1 and R_2 peaks.

Pressure calibration with the gold internal standard was performed by fitting a single cubic a parameter to the 111, 220, and 311 peaks of the gold calibrant, employing a pseudo-Voigt peak profile. The gold 200 peak frequently overlapped with a strong gasket-scattering peak, and was disregarded. The literature values for the compressibility and ambient-pressure unit-cell volume of gold did not agree perfectly with the results of the pressure calibration, and so we used a gold equation of state obtained from our data.

E. XRD sample data analysis

1. Structure refinement

The crystal phases of each nanoparticle sample were verified with full profile refinement using the GSAS code.[20] As described below, lower-symmetry modifications of the bulk ZnS structures were required to satisfactorily fit the XRD data.

2. Unit-cell volume vs pressure

Once an acceptable structure was decided upon, analysis of the XRD compressibility study was performed using routines written in IGOR PRO. A simulated diffraction pattern was fitted to the sample data to obtain the variation of the sample lattice parameter(s) with applied pressure. The single-peak contribution is

$$\Gamma_i(2\theta) = I_i\left[1 - A_S\frac{\Delta T^2}{\tan\theta}\right]V(\Delta T, \sigma, \eta),$$

where $\Delta T = 2\theta_{peak\ i} - 2\theta$, A_S is an asymmetry parameter, V is a normalized pseudo-Voigt peak for which the Gaussian-Lorentzian ratio is given by η, and the peak width is defined by $\sigma^2 = U\tan^2\theta + V\tan\theta + W$, where U, V, and W are numerical parameters. All peak-width and asymmetry parameters were required to fit the diffraction patterns from the smallest nanoparticles.

In addition to the calculated diffraction pattern, a three-parameter background-scattering curve was fitted. The background function is based upon the Debye equation for a single interatomic bond length.[21] For the 2θ range analyzed, this function gave better results to the background scattering from nanoparticle samples than a polynomial function of 2θ for the same number of parameters,

$$I_{BG}(2\theta) = \text{offset} + I_0\frac{\sin(Qr)}{Qr},$$

where $Q = 4\pi/\lambda\sin(\theta)$ and r is an interatomic distance. Typically, fitted $r = 2.0$–2.3 Å, close to the Zn-S bond length in the cubic and hexagonal forms of ZnS (2.34 Å).

A 2θ offset is frequently included during the XRD pattern refinement acquired in Bragg-Brentano geometry with a scanning detector, but is not physically justified for transmission geometry with a 2D detector, for which the dominant positioning errors involve the determination of the beam center. When a 2θ offset was allowed to vary during an analysis of the compression of the ZnS bulk standard, the offset was found to vary randomly about zero with a root-mean-squared value of 10^{-3} deg. Thus, no offset was fitted during data analysis.

3. Equation-of-state fitting

The Birch-Murnaghan equation of state is widely used to describe the compression of a material in response to an applied hydrostatic pressure P (Refs. 22 and 23). It is derived from a Taylor expansion of the strain energy of a continuum elastic body. To third order in Eulerian strain it is written

$$P = \frac{3}{2}B\left[\left(\frac{V}{V_0}\right)^{7/3} - \left(\frac{V}{V_0}\right)^{5/3}\right] \times\left\{1 - \frac{3}{4}(4 - B')\left[\left(\frac{V}{V_0}\right)^{2/3} - 1\right]\right\},$$

where V/V_0 is the ratio of the pressurized to ambient unit-cell volumes, B is the compressibility, and B' is the pressure derivative of the compressibility: $B' = dB/dP$. As discussed below, the data quality was not sufficient to permit B' to be stably fitted, and hence this parameter was fixed at $B' = 4$, for which the equation of state reduces to its second-order form,

$$P = \frac{3}{2}B\left[\left(\frac{V}{V_0}\right)^{7/3} - \left(\frac{V}{V_0}\right)^{5/3}\right].$$

The lattice parameters obtained from fits to XRD patterns from each nanoparticle sample had significant errors associated with the broad-peak profiles and uncertainty in the exact nature of the crystal structure. Consequently, the ambient-volume unit-cell parameter was treated as a free variable during equation-of-state fitting.

III. RESULTS

A comparison of XRD peak positions for bulk ZnS and the MER sample of ZnS nanoparticles reveals visually the presence of a noncubic distortion [Fig. 1(a)]. The dominant diffraction peaks [indexed as the (111), (220), and (311) peaks in the sphalerite phase] are not equally shifted with respect to the corresponding peaks for bulk ZnS. While this effect is greatest for the MER sample, it was observed in all nanoparticle samples when refinement of the diffraction data was performed.

For the sphalerite phase, lower-symmetry subgroups offering an additional degree of freedom are *tetragonal* ($a = b \neq c$; $\alpha = \beta = \gamma = 90°$) and *rhombohedral* ($a = b = c$; $\alpha, \beta, \gamma \neq 90°$).[24] As shown in Fig. 1(a), both structures gave a better fit to the XRD patterns from ZnS nanoparticles. The goodness of fit was slightly better for the tetragonal structure, which was consequently used to obtain the pressure-dependent equations of state. The distorted MER structure is compared with sphalerite in Fig. 1(b).

Figure 2 shows an example of the fit to the XRD data for bulk ZnS at a high pressure point (~8 GPa). The ruby-emission spectrum obtained for the same pressure point shows two clearly resolved lines, indicating that the compressibility study was performed under quasihydrostatic con-

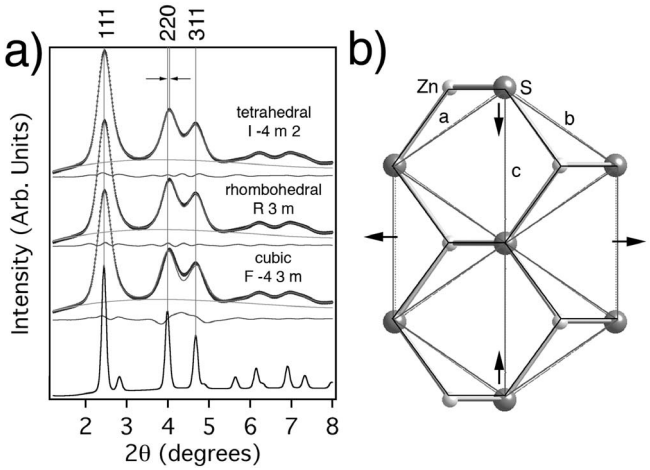

FIG. 1. Determining the best-fit structure for 3-nm-diameter ZnS nanoparticles with mercaptoethanol coating. (a) Full-profile XRD refinement of high-energy powder-diffraction data using cubic, rhombohedral, and tetrahedral settings for the sphalerite structure. The lowest curve is bulk ZnS with perfect cubic sphalerite structure. As shown by the arrows (top) and the residuals, the principal three peaks in the nanoparticle data are not simultaneously fit by a cubic structure. (b) A comparison of the bulk cubic structure and the fitted tetragonal distortion. The gray-scale ball-and-stick model shows the tetragonal structure. The initial cubic structure is superimposed as black lines. Solid (dashed) lines represent the tetragonal (cubic) unit cell. Arrows indicate the directions of the principal structural distortions.

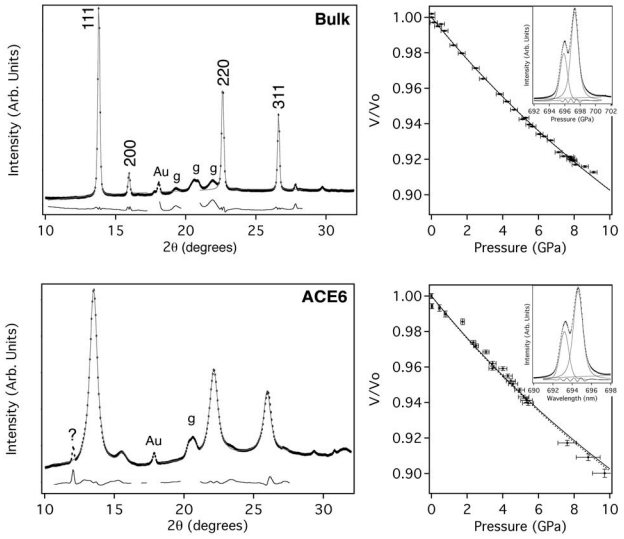

FIG. 2. The compressibility of bulk cubic (sphalerite) ZnS (top) and 6.2-nm-diameter "ACE6" ZnS nanoparticles with a nominally cubic structure (bottom). The left-hand graph shows an example full-profile fit to the diffraction data. "Au" labels scattering from internal gold calibrant; "g" labels gasket scattering. Gaps in the residuals below the data curves indicate regions of masked data excluded from the fit. The right column shows the equation of state (EOS) fit (dotted line) to the fitted reduced unit-cell volume (markers) as a function of pressure. The bulk ZnS EOS, derived from Desgreniers *et al.*, is shown as a solid line. Inset: Ruby fluorescence spectrum (markers) and fit for the same pressure as the XRD pattern on the left.

ditions. The experimental equation of state fitted to the pressure dependence of the relative unit-cell volume exactly overlaps that obtained by Desgreniers *et al.* (Ref. 25), confirming that the bulk modulus of bulk ZnS is 79.5±0.9 GPa. In both cases, B was obtained assuming $B'=4$.

Figure 2 additionally gives the results for 6.2-nm-diam ZnS nanoparticles, which exhibit a compressibility that is indistinguishable from that of bulk ZnS. In contrast, as shown in Fig. 3, every smaller ZnS nanoparticle is clearly more compressible than bulk ZnS. Figure 4 gives the results for a sample of 4.8 nm ZnS nanoparticles nominally in the hexagonal wurtzite structure. As above, XRD refinement using the hexagonal setting could not give satisfactory agreement with all peaks, and we fitted the experimental data with the lower-symmetry *orthorhombic* space group. The fitted bulk moduli of all samples are summarized in Table I.

IV. DISCUSSION

A. Ambient structure and stability of nanoparticles

A full description of the structure of nanoparticles should comprise the underlying crystal phase (determined from full-profile XRD refinement), degree of interior disorder (estimated from the XRD peak width while accounting for particle size), and the surface structure (which remains experimentally inaccessible). There is considerable uncertainty associated with each of these aspects of nanoparticle structure. For example, one cannot say with confidence that either the tetragonal or rhombohedral setting is a better representation of the true structure of the nominally cubic nanoparticles. Moreover, it has been shown that the interpretation of nanoparticle structure using Bragg's theory of lattice diffraction can be inherently misleading, because finite-particle size alone can modify the absolute positions of XRD peaks.[26] However, the differences between XRD data from ZnS nanoparticles and bulk ZnS cannot be explained by finite-size effects alone, and we conclude that they represent a true structural modification. Despite these considerations, the determination of compressibility is weakly dependent upon the choice of structural model, and more detailed analyses (if available) would be unlikely to change the principal results of this study.

During the study of nanoparticles, it is frequently discovered that the structure obtained by a particular synthesis method is not the thermodynamically most stable one.[27] In such a case, unanticipated phase transitions may occur upon the application of pressure, and it is well known that compressibility studies in the vicinity of phase transitions may be inaccurate. For example, one study of wurtzite ZnS nanoparticles observed a transformation to sphalerite that was not reversible upon decompression.[28] A deficiency of the present study is thus the lack of accurate decompression data, which helps to verify the stability of the material studied. In almost every experimental run, deformation of the gasket occurred at elevated pressure, and the consequent inclusion of gasket scattering made accurate XRD fitting impossible. However, in all cases, the XRD patterns after decompression closely

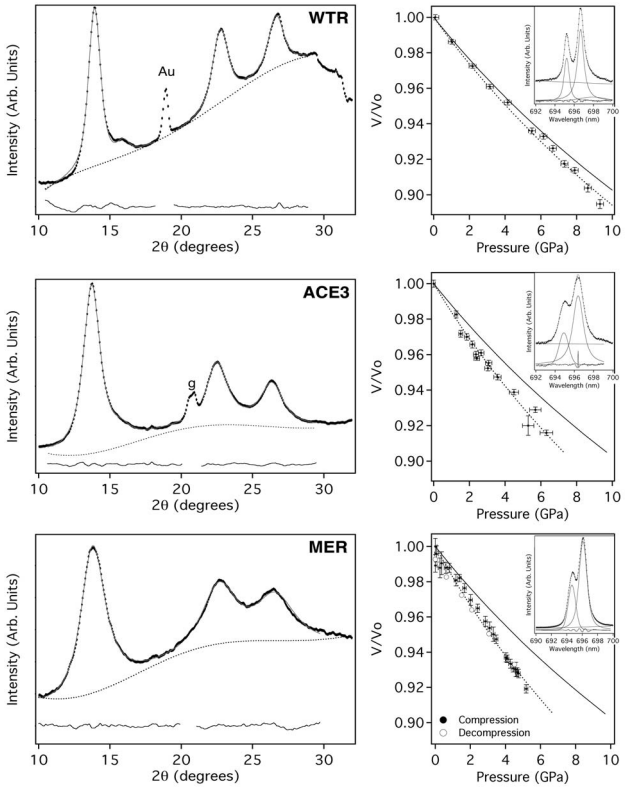

FIG. 3. The compressibility of three samples of ZnS nanoparticles with a nominally cubic (sphalerite) structure. The nanoparticles differ in their apparent size and surface chemistry. (See Fig. 2 for the legend.)

matched the initial ambient data. Furthermore, no phase transitions were observed in the pressure range studied. In all published data,[9,10,25] and in additional studies by our group, no nominally cubic ZnS nanoparticle sample underwent a phase transition below 15 GPa.

To summarize, in this work we assume that the nanoparticles studied are in the most stable conformation for their specific size and surface chemistry. Previous work has shown the structure of ZnS nanoparticles to be responsive to changes in surface environment,[4,5] indicating that these materials are able to adopt a low-energy configuration at room temperature.

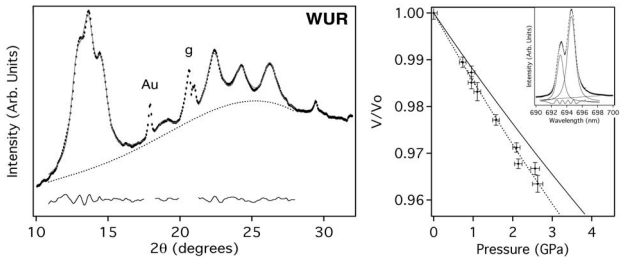

FIG. 4. The compressibility 4.8-nm-diameter ZnS nanoparticles with a nominally hexagonal (wurtzite) structure. (See Fig. 2 for the legend.)

TABLE I. Summary of particle size estimated from XRD peak-width broadening, crystallographic space group, ambient unit-cell volume (V_0), and best-fit compressibility for bulk and nanoscale ZnS.

Sample	Particle size (nm)	Space group	Ambient tetragonal V_0 (Å^3)[a]	Compressibility (GPa)
Bulk	>100	$F43m$	79.0±0.05	79.5±0.9
ACE6	6.2	$I4m2$	77.5±0.2	78.3±2.2
WTR	3.8	$I4m2$	78.3±0.4	71.4±1.0
ACE3	3.2	$I4m2$	78.2±0.5	59.7±4.6
MER	1.6	$I4m2$	77.4±0.3	55.1±2.0
WUR	4.8	$Cmc2_1$		66.2±4.7

[a]The bulk cubic ZnS unit-cell volume is calculated using a tetragonal setting to permit comparison.

B. Structural changes with pressure

In addition to unit-cell compression, we observed changes in the nanoparticle crystal structure as a function of applied pressure. The structure of each nanoparticle sample becomes less cubic with pressure, and this trend is shown in Fig. 5(a) by plotting the ratio a_{cubic}:$a_{\text{tetragonal}}$. The cubic unit-cell a parameter is calculated from the unit-cell volume assuming a cubic structure. The tetragonal a parameter is obtained directly from the XRD refinement. With the exception of the MER sample, the trends for all the nominally cubic nanoparticles are very similar.

C. Trends in the compressibility of ZnS nanoparticles

Among the nominally cubic nanoparticles there is an approximate correlation between their compressibility and their

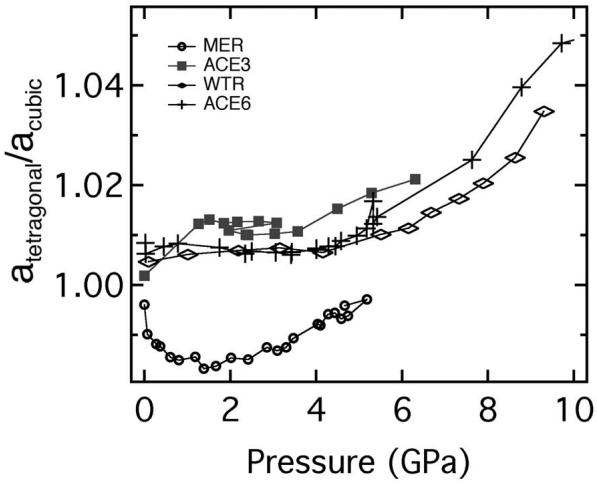

FIG. 5. The variation of the noncubic distortion as a function of pressure. The fitted tetragonal unit-cell volume is used to calculate the a parameter that would be expected if the particles possessed perfect cubic symmetry. For perfect cubic symmetry, $a_{\text{tetragonal}}/a_{\text{cubic}}=1$. Error bars (approximately ±0.005 units on the y axis) are suppressed for clarity.

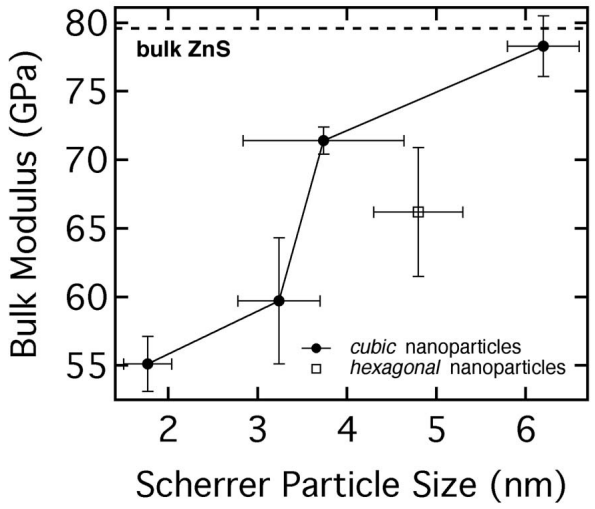

FIG. 6. The variation in the bulk modulus of ZnS nanoparticles with a nominally cubic structure as a function of particle size derived from the Scherrer analysis of the XRD peak widths at ambient pressure. The errors in the particle size are the standard deviation in the mean particle size calculated from the (111), (220), and (311) peaks.

ambient-pressure unit-cell volume. This observation is counterintuitive: these nanoparticles not only exhibit compressed unit-cell volumes relative to the bulk material under ambient conditions, but are compressed more rapidly with increasing pressure.

We also sought the trend in compressibility with particle size. There are numerous methods of nanoparticle size determination, including TEM imaging, UV-vis absorption spectroscopy, small-angle x-ray scattering (SAXS), and XRD peak-width broadening. We used the Scherrer method for estimating the apparent particle size. While it is difficult to separate the peak-broadening contributions from finite size and structural disorder, this provided a consistent measure for all nanoparticles studied. As shown in Fig. 6, there is a dramatic increase in compressibility when particle diameters are less than ~6 nm.

D. Relation to previous studies

We previously conducted a combined x-ray scattering and temperature-dependent extended x-ray-absorption fine-structure (TD-EXAFS) study of the sample MER (the same sample and batch studied here).[3] We found both considerable interior disorder and lattice contraction in the ambient-pressure structure of this ZnS nanoparticle by analysis of the real-space pair-distribution function (PDF). Furthermore, these structural modifications were correlated with an increase in the effective Debye-Waller temperature Θ_T for vibrations of the Zn-S bond. The same effect has been observed in nanoparticles of CdSe (Ref. 29) and Au,[30] and has been termed *contraction-driven stiffening* because an increased Θ_T corresponds to a reduction in the amplitudes of thermal vibrations at a given temperature. It is a great surprise, therefore, to discover that this sample is the *most compressible* out of all the nanoparticle samples studied here.

TD-EXAFS probes the dynamic (high-frequency-weighted) vibrational density of states, and is a measure of the repulsive force between atom pairs. By contrast, HP-XRD measures the zero-frequency compliance of a structure to an isotropic mechanical stress. Bond shortening is not the only mechanism to achieve volume reduction in a structure; there are additional modes of structural compliance. For stoichiometric, ordered bulk materials with open framework structures, bond bending can be an important response to pressure. Comparisons between amorphous and crystalline materials of the same stoichiometry reveal the contributions of a material's structure to its rigidity. For example, bulk crystalline quartz (SiO_2) exhibits a relatively low bulk modulus that is due to *bond bending* rather than *bond contraction*: individual Si-O bond distances change very little over a large pressure range.[31] The compressibility of bulk amorphous SiO_2 is very close to that of the crystalline phase because its structural response to applied pressure is the same.

An alternative mechanism can occur if a material contains many defects. The application of pressure could lead to the expulsion of vacancies, especially for nanoscale materials in which defects are always close to the surface. Bulk ZnS is known frequently to be slightly nonstoichiometric.[32] Although we do not know the accurate stoichiometry of our samples, it is plausible that the Zn:S ratio diverges from unity to a greater extent in ZnS nanoparticles.

In contrast to a structural response based on bond bending, vacancy elimination would be an irreversible process. Experimental problems prevented the acquisition of decompression data for most samples, but Fig. 3 shows that the compression of the MER sample was reversible to within experimental uncertainty. Furthermore, XRD data were acquired for all samples following complete decompression, and no differences were observed relative to the initial ambient data.

Therefore, we conclude that within ZnS nanoparticles there are additional structural responses for mechanical compliance than can be tolerated in bulk ZnS. Figure 5 shows that increasing pressure distorts the nanoparticle structure further away from the bulk cubic phase, indicating that there must be bond torsion in addition to bond contraction. We speculate that the excess compliance of nanoparticles is a consequence of (i) the lack of long-range stabilizing interactions and (ii) the presence of a nonuniform strain field within the nanoparticles. Molecular modeling will be required to visualize both the structure and structural response of nanoparticles.

V. CONCLUSIONS

Small particle size has numerous consequences for the detailed structure of nanoparticles. We show that small particle size additionally permits additional modes of structural response to applied pressure, leading to increased compressibility in ZnS nanoparticles smaller than 6 nm in diameter. This effect is strongly size dependent, as 6 nm nanoparticles exhibit a compressibility that is indistinguishable from bulk ZnS, while smaller particles show up to a 40% reduction in bulk modulus.

Considerable work remains to obtain a coherent description of the structure, mechanical, and vibrational properties of materials in the sub-5-nm-size range. This goal will be aided by future HP-XRD studies in which the nanoparticle lattice parameters are determined with sufficient accuracy to permit the pressure derivative of the compressibility B' to be determined.

ACKNOWLEDGMENTS

High pressure x-ray diffraction studies were performed at beamline 11.3.1 of the Advanced Light Source (ALS). We thank Sirine Fakra, Arianne Gleason, Sander Calder, and Simon Clark for beamtime support. Raymond Jeanloz and Kanani Lee provided invaluable guidance and equipment at the start of this project. The high-energy x-ray-scattering data were acquired at beamline 11-ID-B at the Advanced Photon Source (APS) with the support of Yang Ren. Funding for this work was provided by the Department of Energy Chemical Sciences Program Grant No. ER 15218 and the National Science Foundation NIRT program Grant No. EAR0123967 and by the Director, Office of Science, of the U.S. Department of Energy under Contract No. DE-AC02-05CH11231. The ALS is supported by the Director, Office of Science, Office of Basic Energy Sciences, of the U.S. Department of Energy under Contract No. DE-AC02-05CH11231. Use of the APS was supported by the U.S. Department of Energy, Office of Science, Office of Basic Energy Sciences, under Contract No. W-31-109-ENG-38.

[1] X. J. Chen, H. F. Xu, N. S. Xu, F. H. Zhao, W. J. Lin, G. Lin, Y. L. Fu, Z. L. Huang, H. Z. Wang, and M. M. Wu, Inorg. Chem. **42**, 3100 (2003).
[2] Y. Zhao, Y. Zhang, H. Zhu, G. C. Hadjipanayis, and J. Q. Xiao, J. Am. Ceram. Soc. **126**, 6874 (2004).
[3] B. Gilbert, F. Huang, H. Zhang, and J. F. Banfield, Science **305**, 651 (2004).
[4] H. Zhang, B. Gilbert, F. Huang, and J. F. Banfield, Nature (London) **424**, 1025 (2003).
[5] B. Gilbert, F. Huang, Z. Lin, C. Goodell, H. Zhang, and J. F. Banfield, Nano Lett. **6**, 605 (2006).
[6] M. Haase and A. P. Alivisatos, J. Phys. Chem. **96**, 6756 (1992).
[7] S. H. Tolbert and A. P. Alivisatos, Annu. Rev. Phys. Chem. **46**, 595 (1995).
[8] S. H. Tolbert and A. P. Alivisatos, Science **265**, 373 (1994).
[9] Y. Pan, S. Qu, S. Dong, Q. Cui, W. Zhang, X. Liu, J. Liu, B. Liu, C. Gao, and G. Zou, J. Phys.: Condens. Matter **14**, 10487 (2002).
[10] S. B. Qadri, E. F. Skelton, A. D. Dinsmore, J. Z. Hu, W. J. Kim, C. Nelson, and B. R. Ratna, J. Appl. Phys. **89**, 116 (2001).
[11] S. B. Qadri, J. Yang, B. R. Ratna, E. F. Skelton, and J. Z. Hu, Appl. Phys. Lett. **69**, 2205 (1996).
[12] W. Vogel, P. H. Borse, N. Deshmukh, and S. K. Kulkarni, Langmuir **16**, 2032 (2000).
[13] K. Sooklal, B. S. Cullum, S. M. Angel, and C. J. Murphy, J. Phys. Chem. **100**, 4551 (1996).
[14] H. Zhang, B. Chen, B. Gilbert, and J. F. Banfield, J. Mater. Chem. **16**, 249 (2006).
[15] P. J. Chupas, X. Qiu, J. C. Hanson, P. L. Lee, C. P. Grey, and S. J. L. Billinge, J. Appl. Crystallogr. **36**, 1342 (2003).
[16] M Chai and J. M. Brown, Geophys. Res. Lett. **23**, 3539 (1996).
[17] A. P. Hammersley, ESRF Internal Report No. ESRF98HA01T, FIT2D V9.129 Reference Manual V3.1, 1998 (unpublished).
[18] A. P. Hammersley, S. O. Svensson, A. Thompson, H. Graafsma, Å. Kvick, and J. P. Moy, Rev. Sci. Instrum. **66**, 2729 (1995).
[19] A. P. Hammersley, S. O. Svensson, M. Hanfland, A. N. Fitch, and D. Häusermann, High Press. Res. **14**, 235 (1996).
[20] A. C. Larson and R. B. von Dreele, Los Alamos National Laboratory Report No. LAUR 86-748, 2004 (unpublished).
[21] A. Guinier, *X-ray Diffraction in Crystals, Imperfect Crystals and Amorphous Bodies* (W. H. Freeman & Co., San Francisco, 1963).
[22] R. T. Angel, Rev. Mineral. Geochem. **41**, 35 (2000).
[23] R. Jeanloz, Phys. Rev. B **38**, 805 (1988).
[24] *International Tables For Crystallography*, Vol. A, edited by Th. Hahn (Springer, Dordrecht, 2002).
[25] S. Desgreniers, L. Beaulieu, and I. Lepage, Phys. Rev. B **61**, 8726 (2000).
[26] B. Palosz, E. Grzanka, S. Gierlotka, S. Stel'Mahk, R. Pielaszek, U. Bismayer, J. Neuefeind, H. P. Weber, and W. Palosz, Acta Phys. Pol. A **102**, 57 (2002).
[27] J. M. McHale, A. Auroux, A. J. Perotta, and A. Navrotsky, Science **277**, 788 (1997).
[28] B. Chen, H. Zhang, and J. F. Banfield (unpublished).
[29] J. Rockenberger, L. Tröger, A. L. Rogach, M. Tischer, M. Grundmann, A. Eychmüller, and H. Weller, J. Chem. Phys. **108**, 7807 (1998).
[30] M. A. Marcus, W. Flood, M. Steigerwald, L. Brus, and M. Bawendi, J. Phys. Chem. **95**, 1572 (1991).
[31] L. Levien, C. T. Prewitt, and D. J. Weidner, Am. Mineral. **65**, 920 (1980).
[32] S. D. Scott and H. L. Barnes, Geochim. Cosmochim. Acta **36**, 1275 (1972).